remote sensing

MDPI

Article

Prior Position- and ZWD-Constrained PPP for Instantaneous Convergence in Real-Time Kinematic Application

Xu Tang [1,*], Shuanggen Jin [1,2] and Gethin Wyn Roberts [3,4]

[1] School of Remote Sensing & Geomatics Engineering, Nanjing University of Information Science & Technology, Nanjing 210044, China; sgjin@shao.ac.cn
[2] Shanghai Astronomical Observatory, Chinese Academy of Sciences, Shanghai 200030, China
[3] Department of Land and Sea Mapping, Faroese Environment Agency, 165 Tórshavn, Faroe Islands; gethinr@us.fo
[4] Faculty of Science and Technology, University of the Faroe Islands, 100 Tórshavn, Faroe Islands
* Correspondence: Xu.Tang@nuist.edu.cn; Tel.: +86-198-5140-3763

Abstract: PPP using Kalman filter typically takes half an hour to achieve high positioning precision, which is required for small movements detection. Many dataset gaps due to temporary GPS receiver signal loss challenge the feasibility of PPP in GPS applications for kinematic precise positioning. Additional convergence time is needed before PPP reaches the required precision again. In this study, Partial parameters were estimated by using the position and ZWD as prior constraint. The solved partial parameters were applied to initialize the Kalman filter for PPP instantaneous re-convergence. A set of bridge GPS data with logging gaps were used to validate the re-convergence performance of improved PPP. The results show that the displacements from position-constrained PPP with initialized variance are 0.14 m, 0.09 m and 0.05 m, which are much better than those from standard PPP. The precision of displacement from position- and ZWD-constrained PPP with initialized variance is slightly improved when compared with that from position-constrained PPP with initialized variance at all 3 surveying points. The bridge experiment verifies that the displacement time series of improved PPP instantaneously converges at the first epoch of all signal reacquired, in contrast, standard PPP deviates by meters. This finding suggests that improved PPP can successfully deal with the GPS data logging gaps for instantaneous convergence.

Keywords: precise point positioning; instantaneous convergence; bridge displacement monitoring; GPS

Citation: Tang, X.; Jin, S.; Roberts, G.W. Prior Position- and ZWD-Constrained PPP for Instantaneous Convergence in Real-Time Kinematic Application. *Remote Sens.* **2021**, *13*, 2756. https://doi.org/10.3390/rs13142756

Academic Editor: Addabbo Pia

Received: 6 June 2021
Accepted: 9 July 2021
Published: 13 July 2021

1. Introduction

Precise point positioning (PPP) has been developed for centimeter-level precision with only one receiver and is supported by International GNSS (Global Navigation Satellite Systems) Service (IGS) products [1]. This technology has been successfully applied in a number of applications, including orbit determination [2,3], precise navigation [4], and GPS meteorology [5]. Atmospheric effect could cause tens of meters delays, which further reduce the PPP positioning precision. Precise water vapor radiometer readings could be applied for improving the PPP precision [6]. The ionosphere-free combination based on dual frequency were generally applied for reducing the severe ionospheric delay. Multi-GNSS is also an optional approach for improving the performance of convergency [7]. Those studies rely on the continually tracked signals. Considerable time is required for PPP to converge to a reasonable position precision. GPS multipath fades the quality of measurements. The severe fading event can introduce satellite measurement outage [8], which will reduce the PPP position precision. In a specific condition, the vehicle GPS data will have a gap while the vehicle pass through a tunnel. The data gaps in GPS signals result in long convergence times for PPP and the failure to give a precise position during the PPP convergence period. This issue reduces the feasibility of using PPP in precise

displacement monitoring applications. Many different methods have been investigated to improve the ambiguity resolution (AR) and shorten the position convergence time. Uncalibrated phase delays are considered to destroy the integer property of carrier phase, and then retrieved for PPP ambiguity resolution [9,10]. The ionospheric delay changes slowly with time, and it can be precisely predicted and used as a constraint for shortening the PPP AR time [11]. The strong scintillation can also degrade the PPP positioning precision. Proper weights applied for least square stochastic model can significantly improve the PPP positioning precision [12]. Instantaneous cycle slip fixing has also been investigated for fast PPP convergence [13]. The cycle slip fixing approach benefits from small changes in the ionospheric delay over short periods. However, these methods cannot address the gaps, which can be up to tens of minutes in duration. A local dense CORS (Continuously Operating Reference Stations) network is applied for interpolating both tropospheric and ionospheric delays. The PPP convergence time has been improved by using the interpolated delays as a constraint [14] instead of using the predicted ionospheric delay. Both predicted and interpolated troposphere PPP require additional computing and communicating functions between the PPP client and correction computing server. In the case of earthquakes, poor atmospheric correction estimates at local CORS stations reduce the practicality of the method.

In a vehicle case, the position can be predicted by other sensors after a short GNSS signal outage. The predicting position from other sensors after GNSS signal reacquired can be used as a constraint for shortening the PPP convergence time. In some PPP applications, the range of movements is also foreseeable. The maximum movement of large suspended bridge decks during time intervals of tens of minutes is approximate 0.5 meters in the vertical direction [15]. The prior position before the data gap occurs can be used as constraint as well in the purpose of shorting PPP convergence. The position, receiver clock offset, zenith wet delay (ZWD) and carrier phase bias are the four types of parameters typically used for standard PPP kinematic estimation and data processing. The receiver clock offset is generally up to tens of nanoseconds, resulting in tens of meter delays in the carrier phase and pseudo-range measurements. The clock offset must be precisely estimated epoch by epoch. Data gaps are the main reason that PPP takes tens of minutes to re-initialize when using the aforementioned four parameters. Previous studies investigated the reacquired carrier phase bias resolution through constraining the atmospheric delays, which are either predicted or interpolated with local CORS station data [11,16].

Kalman filter has been applied in the standard PPP. Long time consumption is required for standard PPP converging a precise position while all GPS signals are reacquired. This study presents a new approach for continuous instantaneous-convergence PPP, which will improve the PPP practicality in the GPS signal frequently interrupted scenario. The obtained partial parameters, at the epoch before the GPS logging gap, are used to establish the receiver clock and carrier phase biases parameters after all signal is reacquired. Then, the established receiver clock and biases at the first epoch of reacquired signal were applied to initialize the Kalman filter for the instantaneous position convergence. Two cases of this method are considered. In the first case, only the prior position is considered as the constraint for improving PPP; in the second case, both the prior position and ZWD are applied for improving PPP for instantaneous convergence after the data logging gap. the variances in partial parameters are also considered in constrained PPP for instantaneous carrier phase bias convergence. The performance of this method, the constrained PPP for dealing with the GPS logging data gaps, is assessed based on an experiment on a long-span suspension bridge, which has evident oscillation.

2. Methods

2.1. Position-Constrained PPP for Instantaneous Convergence

The precise clock and orbit products of GPS satellites play important roles in PPP performance. For the purpose of monitoring a bridge with high-rate oscillation, high-rate satellite clock offset corrections are required [17]. Globally distributed IGS station

measurements with a 1 Hz sampling rate are applied for the estimation of 1 Hz satellite clock corrections. IGS final orbital products, with 15 min intervals between neighboring epochs, are also applied in this study. With this configuration, tens of minutes of data are required for PPP convergence before its precision meets that required for bridge displacement monitoring. The frequent interruption of GPS data gaps reduces the PPP practicality for bridge monitoring.

The gradually changing zenith total delay (ZTD) normally decomposed into the zenith hydrostatic delay (ZHD) and ZWD. The ZHD can be precisely modeled with precision better than 1 mm [18]. The ZWD normally changes within a range of a few centimeters. For an application where there is no large movement and ZWD changing during the dataset gap, such as the displacement monitoring of long-span bridges, the position and ZWD solutions before signal loss can be used as a constraint for the receiver clock and carrier phase bias estimation.

Figure 1 illustrates the flowchart of position- and ZWD- constrained PPP to address the GPS data logging gap between epoch m and epoch n. The receiver clock and zero-differencing carrier phase biases at epoch n can be best solved by using the estimations at epoch m as constraints. Then, the obtained receiver clock and carrier phase bias values will be applied for the precise position estimation at epoch n.

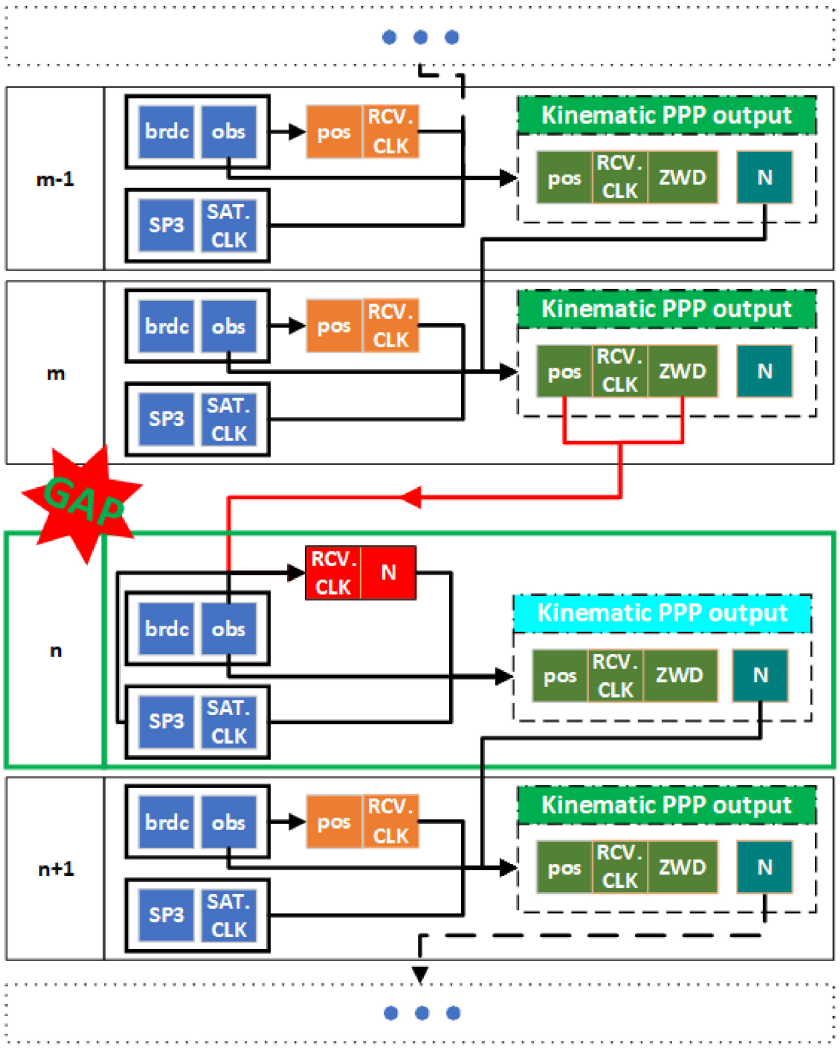

Figure 1. Flowchart of the PPP instantaneous convergence strategy during a data gap. The data gap occurs between epochs m and n. The precise position and ZWD at epoch m can be used as constraints for partial parameters estimation at epoch n.

2.2. Partial Parameter Estimations with Prior Constraints

Considering the receiver clock offset, tropospheric delay and random noise, the zero-differenced observation equation [19] can be written as

$$\varphi_{IF,i}^{j} = \rho_i^j + \tau_i \times c + T_i^j + N_i^j + \xi_i^j \tag{1}$$

where the superscript j and subscript i denote satellite j and receiver i, respectively. φ_{IF} represents an ionosphere-free linear combination carrier phase observation. ρ is the geometric range between the j-th satellite and the i-th receiver. τ is the receiver clock offset. c denotes the speed of light in a vacuum. N denotes the carrier phase bias. ξ is the observation noise, including random noise, high-order ionospheric delays, and multipath errors. T is the tropospheric slant delay of the j-th satellite. An applied mapping function can map all "line-of-sight" slant delays in the zenith direction. With the assumption that k satellites are tracked, k unknown tropospheric delays can be treated as only one unknown zenith total delay by using the mapping function. The Global Mapping Function (GMF) is applied in this study [20]. The slant tropospheric delay can be expressed as

$$T_i^j = M_{zhd,i}^j \times \delta_{zhd,i}^j + M_{zwd,i}^j \times \delta_{zwd,i}^j \tag{2}$$

where the subscripts zhd and zwd are abbreviations of the zenith hydrostatic delay and zenith wet delay, respectively. δ denotes the zenith delay, and M is the mapping function coefficient. The observation equation with unknown partial parameters at epoch n can be written as

$$\boldsymbol{\varphi}_n = \boldsymbol{B} \times \boldsymbol{X}_n + \boldsymbol{\rho}_n + \boldsymbol{T}_n \tag{3}$$

where subscript n denotes the n-th epoch. $\boldsymbol{\varphi}$ is the vector of φ_{IF}. $\boldsymbol{B}$ and $\boldsymbol{X}$, respectively, denote the partial parameter coefficient matrix and partial parameter vector. $\boldsymbol{\rho}$ and $\boldsymbol{T}$ are the vectors of the geometric range ρ and slant tropospheric delay T, respectively.

2.2.1. Case I: Partial Parameter Estimation Using a Position Constraint

In this case, only the position at epoch m is used as the constraint. The partial parameters $\boldsymbol{X}_n$ in (3) include the receiver clock offset, zenith wet delay and ionosphere-free carrier phase biases. With the assumption that there are k tracked satellites and the position constraint, the observation Equation (3) for clock of receiver, ZWD and phase bias solution at epoch n, in matrix formulation, can be written as

$$\begin{bmatrix} \varphi^1 \\ \varphi^2 \\ \vdots \\ \varphi^k \end{bmatrix}_n = \begin{bmatrix} c & M_{zwd}^1 & 1 & & 0 \\ c & M_{zwd}^2 & & 1 & \\ \vdots & \vdots & & & \ddots \\ c & M_{zwd}^k & 0 & & 1 \end{bmatrix} \times \begin{bmatrix} \tau \\ \delta_{zwd} \\ N^1 \\ N^2 \\ \vdots \\ N^k \end{bmatrix}_n + \begin{bmatrix} \rho^1 \\ \rho^2 \\ \vdots \\ \rho^k \end{bmatrix}_n + \begin{bmatrix} T_h^1 \\ T_h^2 \\ \vdots \\ T_h^k \end{bmatrix}_n \tag{4}$$

where random noise and unmodeled noise are ignored. The time-varying zenith wet delay δ_{zwd} is estimated. $\begin{bmatrix} N^1 & N^2 & \dots & N^k \end{bmatrix}^T$ denotes the vector of IF combined phase biases from k satellites. T_h denotes the tropospheric hydrostatic delay. The geometric range vector $\begin{bmatrix} \rho^1 & \rho^2 & \cdots & \rho^k \end{bmatrix}^T$ includes the satellite-receiver distance set computed from the positions of k satellites at epoch n and the receiver antenna position at epoch m.

The variance-covariance matrix of the parameters obtained in (4) can be written as

$$\hat{\boldsymbol{Q}}_n = \boldsymbol{B} \times \boldsymbol{Q}_n \times \boldsymbol{B}^T, \ \boldsymbol{Q}_n = \begin{bmatrix} \sigma_\tau^2 & 0 & \boldsymbol{0} \\ 0 & \sigma_{\delta_{zwd}}^2 & \\ \boldsymbol{0} & & \boldsymbol{\sigma_N^2} \end{bmatrix}_n \tag{5}$$

where variance-covariance matrix $\widetilde{\boldsymbol{Q}}_n$ in (5) is a diagonal matrix that covers the unknown variances of partial parameters. The receiver clock offset variance σ_τ^2, time-varying zenith wet delay variance $\sigma_{\delta_{zwd}}^2$ and phase bias variance along the diagonal of the matrix $\boldsymbol{\sigma_N^2}$ can be either initiated or inherited from the variance-covariance matrix of the parameter at the m-th epoch. The configuration for initializing the diagonal matrix $\widetilde{\boldsymbol{Q}}_n$ in this study is

$$\begin{cases} \sigma_\tau = 30 \\ \sigma_{\delta_{zwd}} = 0.3 \\ \boldsymbol{\sigma_N} = \boldsymbol{I} \end{cases} \tag{6}$$

where $\boldsymbol{I}$ is a $k \times k$ identity matrix. The standard deviation of receiver clock offset is set as 30 meters, the standard deviation of ZWD is set as 0.3 meters.

The diagonal matrix $\widetilde{\boldsymbol{Q}}_n$ can be optionally inherited from that at the m-th epoch,

$$\begin{cases} \sigma_\tau|_n = \sigma_\tau|_m \\ \sigma_{\delta_{zwd}}|_n = \sigma_{\delta_{zwd}}|_m \\ \boldsymbol{\sigma_N}|_n = \boldsymbol{\sigma_N}|_m \end{cases} \tag{7}$$

where the symbol $g|_n$ denotes g at epoch n. g can be σ_τ, $\sigma_{\delta_{zwd}}$ or $\boldsymbol{\sigma_N}$.

2.2.2. Case II: Partial Parameter Estimation Using Position and ZWD Constraints

ZWD changes by a small range over the GPS data gap of a few minutes. Case II takes the prior ZWD into consideration in the PPP constraint in addition to the position, as in Case I. Then, the unknown partial parameters $\boldsymbol{X}_n$ in (3) contain the receiver clock offset and IF carrier phase biases. Equation (3) can be rewritten in matrix formulation as

$$\begin{bmatrix} \varphi^1 \\ \varphi^2 \\ \vdots \\ \varphi^k \end{bmatrix}_n = \begin{bmatrix} c & 1 & & 0 \\ c & & 1 & \\ \vdots & & & \ddots \\ c & \mathbf{0} & & 1 \end{bmatrix} \times \begin{bmatrix} \tau \\ N^1 \\ N^2 \\ \vdots \\ N^k \end{bmatrix}_n + \begin{bmatrix} \rho^1 \\ \rho^2 \\ \vdots \\ \rho^k \end{bmatrix}_n + \begin{bmatrix} T^1 \\ T^2 \\ \vdots \\ T^k \end{bmatrix}_n \tag{8}$$

with the solved partial parameters of the variance-covariance set written as

$$\hat{\boldsymbol{Q}}_n = \boldsymbol{B} \times \boldsymbol{Q}_n \times \boldsymbol{B}^T, \ \ \boldsymbol{Q}_n = \begin{bmatrix} \sigma_\tau^2 & \mathbf{0} \\ \mathbf{0} & \boldsymbol{\sigma_N^2} \end{bmatrix}_n \tag{9}$$

where T in (8) contains the precise modeled tropospheric hydrostatic delay and the wet delay estimated at the m-th epoch. The diagonal matrix $\widetilde{\boldsymbol{Q}}_n$ can be initialized as

$$\begin{cases} \sigma_\tau = 30 \\ \boldsymbol{\sigma_N} = \boldsymbol{I} \end{cases} \tag{10}$$

or inherited from the variance-covariance matrix of estimated parameters at the m-th epoch as

$$\begin{cases} \sigma_\tau|_n = \sigma_\tau|_m \\ \boldsymbol{\sigma_N}|_n = \boldsymbol{\sigma_N}|_m \end{cases} \tag{11}$$

Instead of using only the position as the PPP constraint in Case I, Case II applies both position and ZWD constraints for parameter estimation as soon as all the GPS signal is reacquired.

2.3. PPP Instantaneous Convergence

The obtained partial parameters $\boldsymbol{X}$ and corresponding variance-covariance matrix $\widetilde{\boldsymbol{Q}}$ are used for the instantaneous convergence of PPP. The instantaneous PPP observation equations in Case I and Case II can be written as

$$\boldsymbol{\varphi}_n = \begin{bmatrix} \boldsymbol{\gamma} & \boldsymbol{B} \end{bmatrix} \times \begin{bmatrix} \boldsymbol{X}_{pos} \\ \boldsymbol{X}_{cons} \end{bmatrix}_n + \boldsymbol{\rho}_n + \boldsymbol{T}_{n,h} \tag{12}$$

and

$$\boldsymbol{\varphi}_n = \begin{bmatrix} \boldsymbol{\gamma} & \boldsymbol{M}_{zwd} & \boldsymbol{B} \end{bmatrix} \times \begin{bmatrix} \boldsymbol{X}_{pos} \\ \delta_{zwd} \\ \boldsymbol{X}_{cons} \end{bmatrix}_n + \boldsymbol{\rho}_n + \boldsymbol{T}_{n,h} \tag{13}$$

where $\boldsymbol{\gamma}$ is the set of unit vector from k tracked satellites to the receiver. Kalman filter state vector at epoch n is initialized by approximate receiver position and the solved $\boldsymbol{X}_{cons}$ from Case I or Case II. Meanwhile, the variance-covariance matrixes of Kalman filter state vector can be, respectively, written as

$$\boldsymbol{Q}_n = \begin{bmatrix} \sigma^2_{pos} & \boldsymbol{0} \\ \boldsymbol{0} & \hat{\boldsymbol{Q}}_n \end{bmatrix} \tag{14}$$

or

$$\boldsymbol{Q}_n = \begin{bmatrix} \sigma^2_{pos} & 0 & \boldsymbol{0} \\ 0 & \sigma^2_{\delta_{zwd}} & \\ \boldsymbol{0} & & \hat{\boldsymbol{Q}}_n \end{bmatrix} \tag{15}$$

where $\sigma^2_{pos,n}$ from (14) and (15) is a 3×3 diagonal matrix for which all elements are 900 along the main diagonal. $\sigma_{\delta_{zwd}}$ in (15) is 0.3 in this study.

2.4. Field Experiment for Improved PPP Validation

Position-constrained PPP performance is assessed by using the real data collected for the Severn suspension bridge, UK. The main span of the Severn Bridge is 988 meters long. Data gaps exist in the raw GPS data. This experiment allows the performance of constrained PPP to be assessed in an oscillation situation. Figure 2 shows the locations of the GPS surveying points and the relative positions. The green circle located 1.416 km away from the bridge midspan point B is a reference station, allowing post processing the data in double differenced (DD) kinematic model. Figure 3 shows the surrounding environment of the reference station, which is on the roof of a building nearby the Severn bridge.

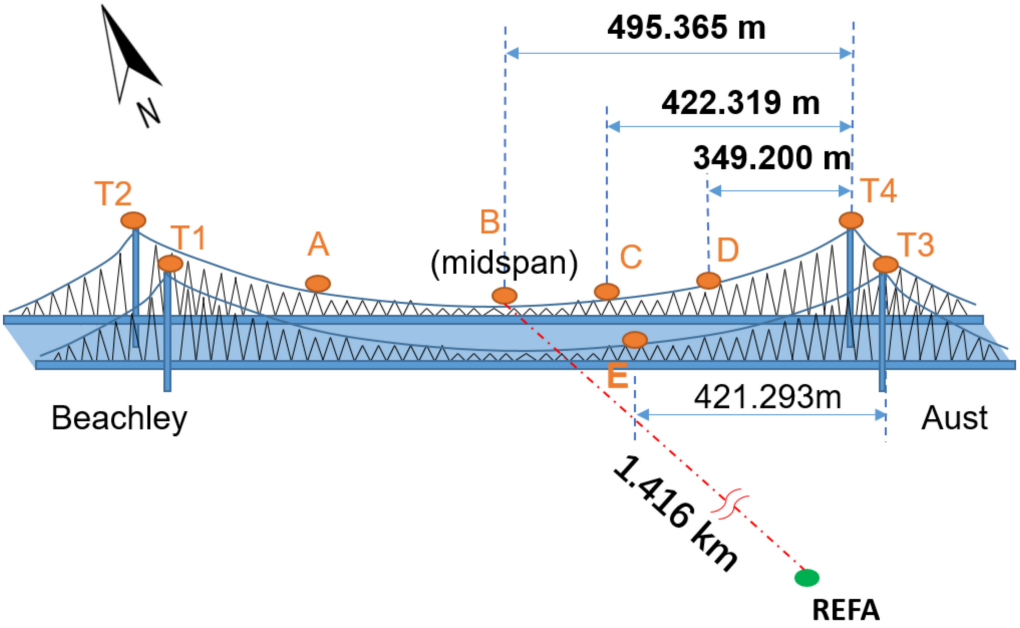

Figure 2. Locations of surveying points on both the suspension cables and the support towers, as well as one reference station, based on the Aust and east sides.

Figure 3. The surrounding environment of GNSS reference station nearby the Severn bridge.

Table 1 shows the locations of GNSS antennas for the various sessions. Eight dual-frequency GPS receivers were mounted on the bridge, including four Leica 1200 receivers mounted on the suspension cables and four Leica SR530 receivers mounted on the supporting towers. The receiver at location D on morning was moved to the location E on afternoon, due to having only limited number of receivers. The antenna we used for the locations A, B, C, D and E are Leica AT503, and AT504 for the locations of T1, T2, T3 and T4. The two reference receivers and choke ring antennas were Leica 1200 and AT504, respectively. Figure 4 shows the choke ring antenna installation on the bridge suspension cable and tower, respectively.

Table 1. Session times, locations and corresponding GNSS receiver types on March 11, 2010.

	A	B	C	D	E	T1	T2	T3	T4
Morning	1200 AT503	1200 AT503	1200 AT503	1200 AT503		SR530 AT504	SR530 AT504	SR530 AT504	SR530 AT504
Afternoon	1200 AT503	1200 AT503	1200 AT503		1200 AT503	SR530 AT504	SR530 AT504	SR530 AT504	SR530 AT504

Figure 4. The illustrations of bridge cable surveying point antenna installation (**left panel**) and tower surveying point antenna installation (**right panel**).

The sampling rate of the four cable-mounted dual-frequency receivers was 20 Hz, and the sampling rates of the receivers mounted on the towers were all 10 Hz. Two reference stations were located within 2 km of the bridge for DD data processing, and their sampling rate was 20 Hz. Only one of the two reference stations was selected for the DD data processing. The one that has not been selected was used as the backup of the selected station, in case of logging data failure. The elevation cut-off angle was set to 5 degrees. Data were collected on two separate occasions, from 10 to 12 March 2010, and again on 18 March 2010. The data were logged on SD cards in the receivers. Approximately every ten hours, the SD cards in the receivers were replaced by a new empty card due to the storage limitations of the memory cards. It is inevitable that gaps occurred because of switching the SD cards. We aim to assess the PPP convergence time when all signal was reacquired. The GPS data for all the survey points from 10:00:00 to 12:00:00 are selected. There are no gaps during this period at surveying point A; towers 1, 2, 3 and 4; or the reference station. Table 2 shows 4 data gaps that occurred at points B, C and D during this survey period. Gap 2 at point B is an artificial gap introduced by manually deleting the observations over a short period (15.3 s). Gaps 1, 3 and 4 occurred due to the SD cards being switched. The sampling rate of all receivers' logging data is reduced to 10 Hz from the original 20 Hz by using TEQC [21]. In-house software was used to produce 1 Hz clock corrections that were applied for high-rate PPP [17].

Table 2. GPS observation gaps at locations B, C and D over the 2 h from 10:00:00 to 12:00:00 on 11 March 2010.

	GAP 1	GAP 2	GAP 3	GAP 4
Point B	-	10:35:31.9- 10:35:47.2 Gap arc: 15.3 sec	-	11:00:32.6- 11:02:02.2 Gap arc: 89.6 sec
Point C	-	-	10:37:08.4- 10:38:22.1 Gap arc: 73.7 sec	-
Point D	10:30:10.0- 10:31:43.1 Gap arc: 93.1 sec	-	-	-

3. Results

3.1. Position, Clock, ZWD and Carrier Phase Bias Solutions from Constrained PPP

Standard PPP, position-constrained PPP and position- and ZWD-constrained PPP were applied to the GPS data at point B covering both the real and artificial gaps illustrated in Table 2. The partial parameter variance-covariance matrices for position-constrained PPP and position- and ZWD-constrained PPP are configured as in (6) and (10), respectively. Figure 5 illustrates the bridge displacement time series from standard PPP, position-constrained PPP, as well as position- and ZWD constrained PPP. Figure 5 (top, middle, bottom), respectively, illustrates the latitudinal, longitudinal and vertical components of bridge displacement at surveying point B. The results confirmed that the artificial data gap does not have a significant impact on standard PPP or constrained PPP. The displacement precision of standard PPP degrades after the data gap, which is due to signal loss. Approximately half an hour of data is generally required for the resulting coordinates to be at a reasonable precision. Both position-constrained PPP and position- and ZWD-constrained PPP have similar convergence performances for the latitudinal, longitudinal and vertical components. The maximum differences between position-constrained PPP and position- and ZWD-constrained PPP are 1.3 cm, 1.5 cm and 3.6 cm, respectively, for the latitudinal, longitudinal and vertical components.

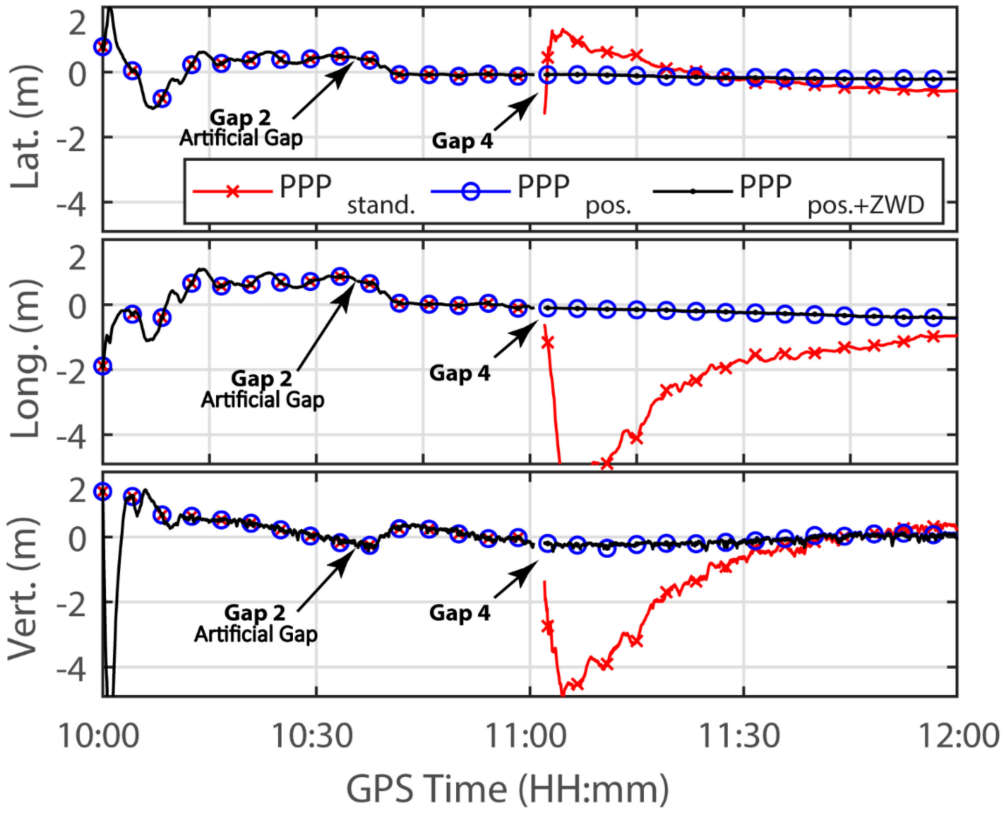

Figure 5. Standard PPP and constrained PPP time series at bridge surveying point B over 2 h for the latitudinal, longitudinal and vertical components.

Figure 6 illustrates the performance for the receiver clock offset, ZWD and GPS PRN11 carrier phase bias solutions over 2 h at point B. Other GPS satellite phase bias solutions from the standard PPP and constrained PPP are presented in the Appendix A (Figure A1). Similar to the position performance, there are no significant differences between position-constrained PPP and position- and ZWD-constrained PPP for the receiver clock and phase bias solutions. The maximum differences in the receiver clock offset and GPS PRN 11 phase bias for both PPP methods are 0.248 ns and 7.44 cm, respectively. However, the receiver clock offset and phase bias from the dual-constrained PPP method are evidently different from those of standard PPP during the first 30 min after all the signal is reacquired. The maximum receiver clock offset difference between standard PPP and position- and ZWD-constrained PPP is 9.38 ns. The maximum difference in GPS PRN 11 phase bias between standard PPP and position- and ZWD-constrained PPP is 4.64 m. The receiver clock offset and phase bias differences both decrease over the first 30 min after all the signal is reacquired. The constrained PPP phase bias converges faster to a relatively stable phase bias compared with that of standard PPP. The ZWD time series from all PPP methods do not illustrate evidence of convergence after all the GPS signal was reacquired.

Constrained PPP with partially solved parameters and an initialized variance-covariance matrix can address the data gaps resulting in position instantaneous convergence (Figure 5). However, the phase bias still takes a few minutes for a reasonably stable value (Figure 6, bottom panel). There other 5 satellites phase biases over this period have also plotted on Figure A1 in Appendix A section. Phase biases from constraint PPP still take a few minutes to converge to a stable level but have a better performance than those from standard PPP. Figure 6 (top) illustrates the estimated receiver clock offsets from standard PPP and constrained PPP. The constrained PPP clock offsets change consistently with the one from standard PPP in terms of high-rate changes. Moreover, there is an evident gradual change in the constrained PPP clock offset compared with that for standard PPP. The gradual changes in both the clock offset and phase bias imply that the constrained PPP with partially solved

parameters and initialized variance-covariance matrix fails to instantaneously converge for the phase bias and receiver clock instantaneous convergence. Contrarily, there is no evidence of ZWD convergence after the data gap occurs. Thus, the ZWD solution does not affect the constrained PPP receiver clock offset and phase bias convergence procedure.

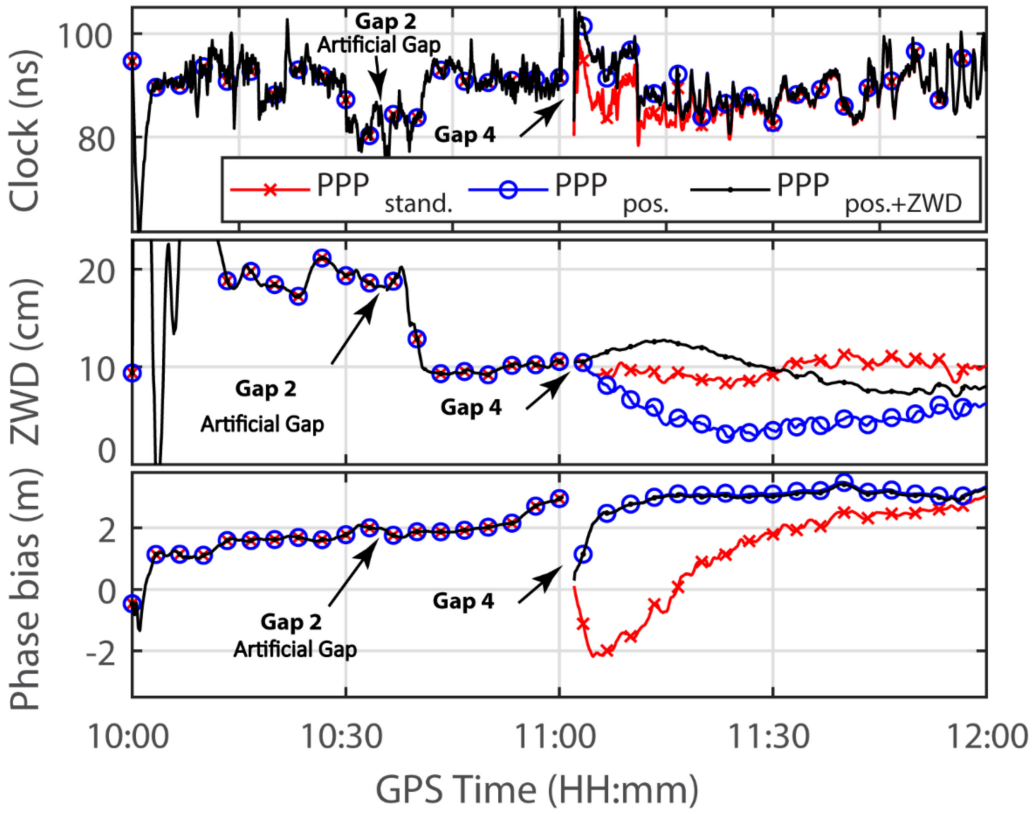

Figure 6. Bridge surveying point B receiver clock, ZWD and tracking GPS satellite phase bias (PRN11) from standard PPP and constrained PPP over 2 h.

3.2. Constrained PPP Performance under the Condition of Inherited Variances

To achieve instantaneous convergence for the receiver clock offset and phase bias over the data gap, the changes in the corresponding variances are taken into consideration. Instead of using the initialized variance of the receiver clock offset and phase bias in (10), the clock offset and phase bias variances in (11) are inherited from those of the PPP parameter solution before the gap occurs. Figure 7 illustrates the variances of receiver clock offset and GPS PRN 11 phase bias, respectively, from the standard PPP and constrained PPP methods. The variance in both standard PPP and position- and ZWD-constrained PPP with initialized partial parameter variance in Figure 7 shows the convergence trend after all the GPS signal is reacquired. The receiver clock offset variance from the position- and ZWD-constrained PPP with inherited variance shows an instantaneous convergence result as soon as all the GPS signal is reacquired. Similar to the receiver clock offset variance, the GPS PRN 11 phase bias variances from standard PPP and constrained PPP with initialized partial parameter variance also have the converge phenomena. The variance in the converging period can be ignored only when the inherited partial parameter variance is applied in constrained PPP.

Figure 8 illustrates the receiver clock offset and GPS PRN 11 phase biases from standard PPP and constrained PPP with the covariance of the initialized or inherited partial parameters. Phase biases from both standard PPP and position- and ZWD-constrained PPP with initialized covariance take time to converge to a stable value, with corresponding phase bias variance convergence in Figure 7 (bottom). Under the conditions of satellite

phase bias variance and receiver clock offset variance, position- and ZWD-constrained PPP displays stable phase bias as soon as all the signal is reacquired. The receiver clock changes are consistent with those from standard PPP but have a relatively constant bias.

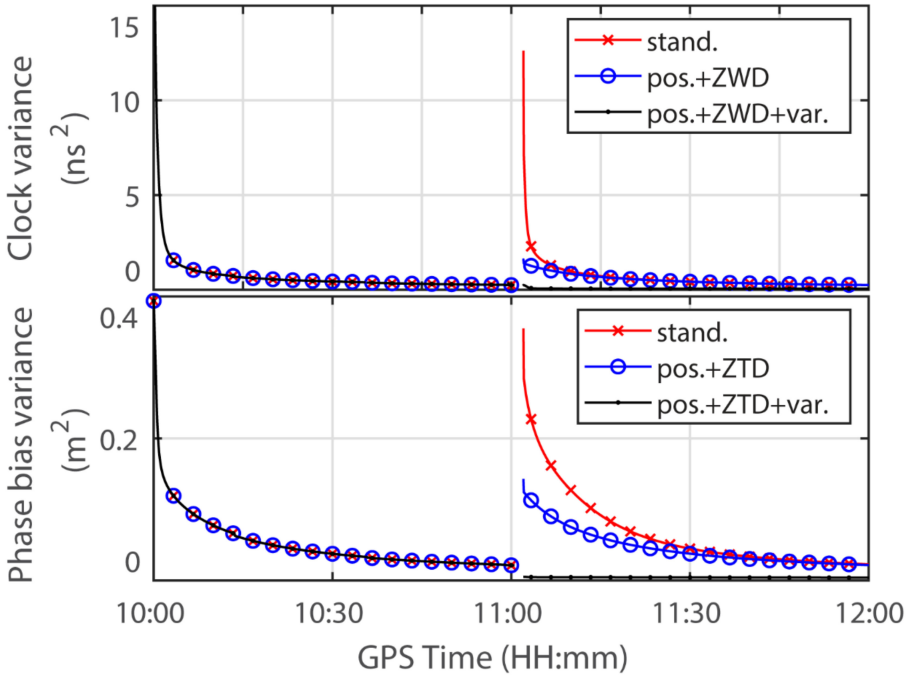

Figure 7. Variance time series for the receiver clock offset and GPS PRN 11 phase bias estimations from the standard PPP (red line with cross marks), position- and ZWD-constrained PPP with initialized variance (blue line with cycle marks) and position- and ZWD-constrained PPP with inherited variance from prior estimations before the gap (black line with solid dots).

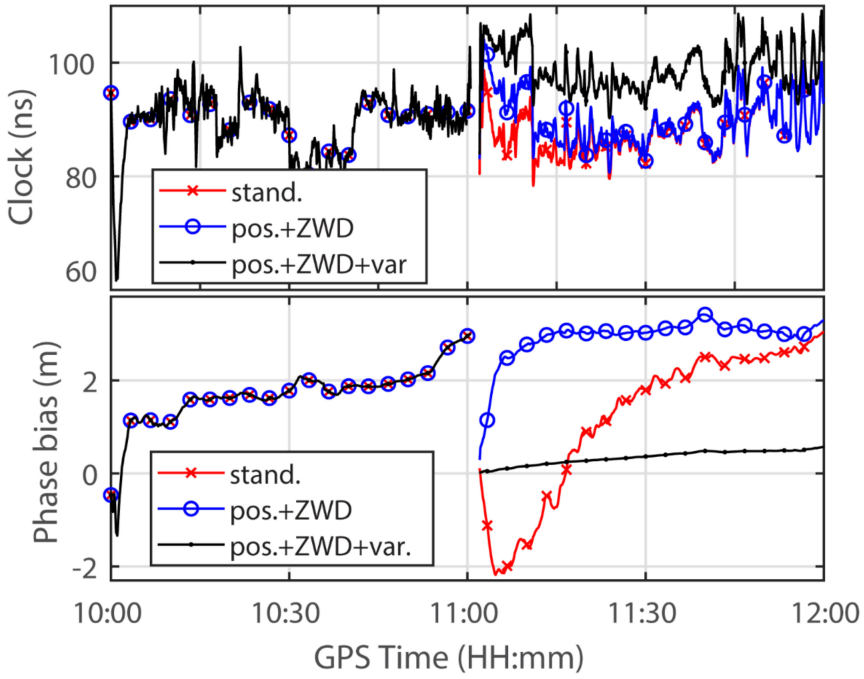

Figure 8. Receiver clock offset and GPS PRN 11 phase bias time series for standard PPP (red line cross marks), position- and ZWD-constrained PPP with initialized variance (blue line with cycle marks), as well as position- and ZWD-constrained PPP with inherited variance from prior estimations before the gap (black line with solid dots).

Figure 9 illustrates the 1-hour-level differences in the receiver clock offsets from standard PPP and position- and ZWD-constrained PPP with the inherited variance. A relatively large difference in clock offsets occurs during the first twenty minutes after all the signal is reacquired. The clock offset difference increases from 3.414 ns to 16.69 ns during the first 2 min and starts to decrease to a stable value range from 8 ns to 10 ns. The difference is quite small compared to the clock offsets from standard PPP or from position- and ZWD-constrained PPP with inherited variance.

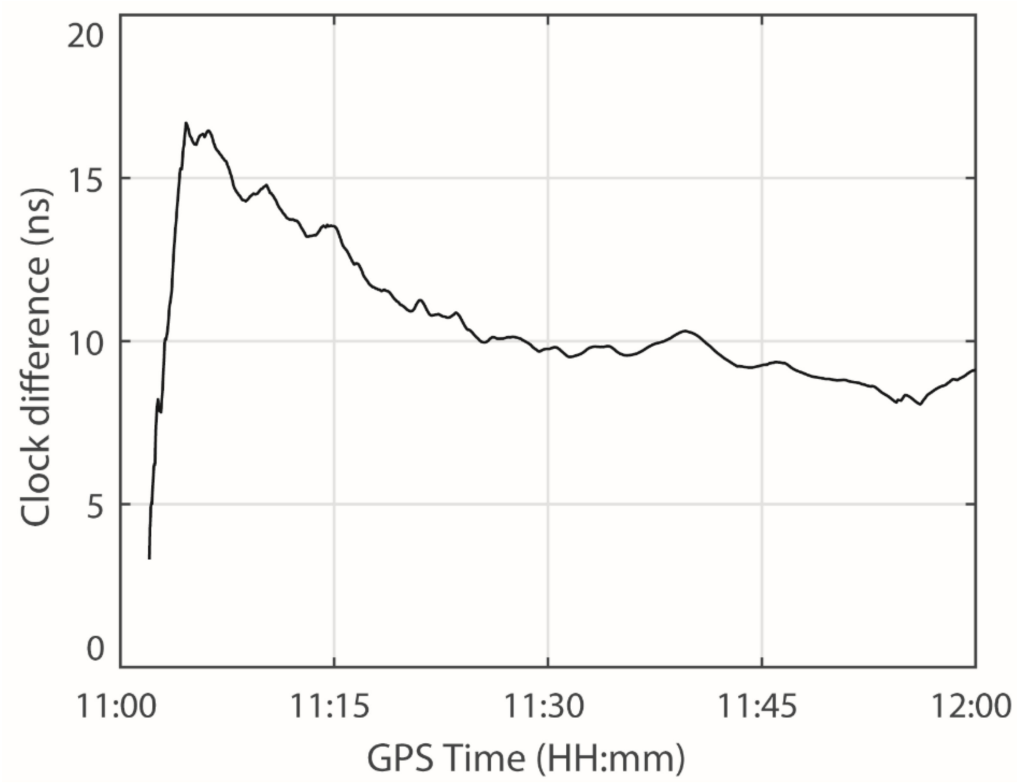

Figure 9. Receiver clock offset difference between standard PPP and position- and ZWD-constrained PPP with inherited variance.

3.3. Performance of Constrained PPP Displacement

The GPS DD is well established for structural displacement monitoring. DD displacements are treated as the true values against which the position-constrained PPP displacement time series is assessed. Figure 10 illustrates the variance-inherited position- and ZWD-constrained PPP displacement time series and those from the DD method and standard PPP at surveying point B. Meanwhile, the results at surveying points C and D could be found in Figure A2 in the Appendix A section. The displacement time series of points B, C and D clearly show peaks, which are due to vehicle weight loads on the bridge. The constrained PPP time series also shows the bridge displacement immediately when all the GPS signal is reacquired. It should be noted that variance-inherited position- and ZWD-constrained PPP bridge displacement also shows gradual changes over almost 1-hour. There is no backward filter introduced for PPP data processing, so that the data analysis is simulating a real-time scenario. As a comparison, standard PPP takes more than half an hour to converge to a reasonable precision for bridge displacement monitoring. Standard PPP displacement time series over the first 40 min does not show the peaks, which are clear in those of DD and constrained PPP.

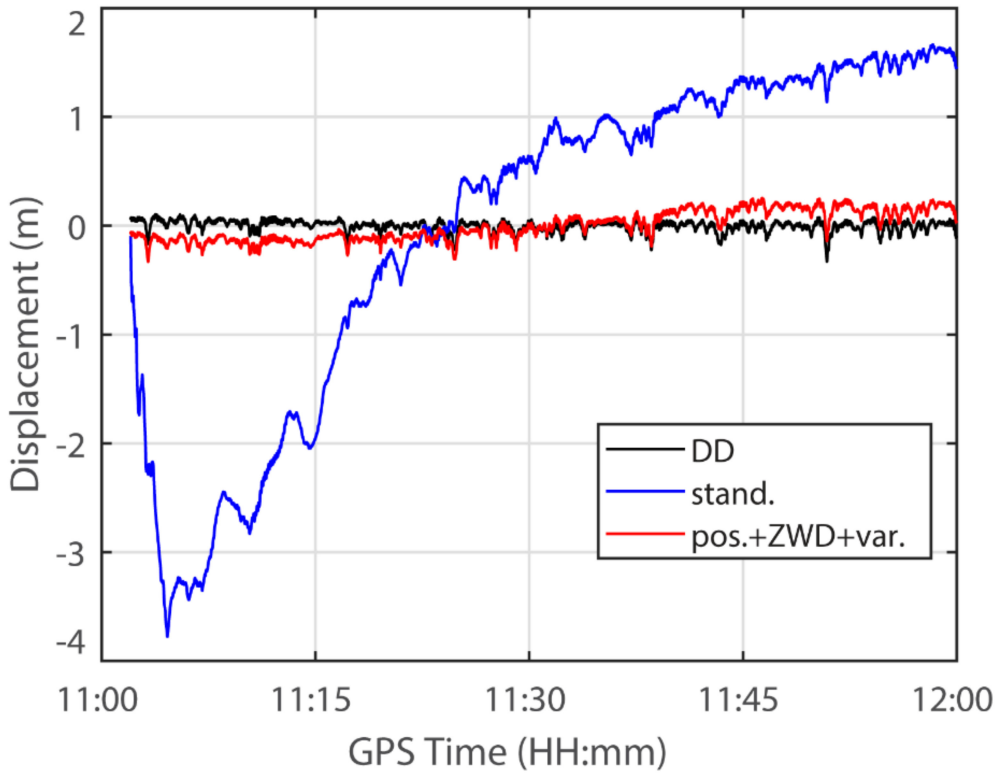

Figure 10. Comparison of position-constrained PPP and DD displacement time series after the data gap at point B.

The DD time series are treated as the truth, and the root mean square errors of standard PPP are 1.55 m, 0.71 m and 0.77 m at points B, C and D, respectively. Table 3 shows the RMSEs of bridge displacements from PPP with different configurations. The displacements from position-constrained PPP with initialized variance are 0.14 m, 0.09 m and 0.05 m, which are much better than those from standard PPP. The precision of displacement from position- and ZWD-constrained PPP with initialized variance is slightly improved when compared with that from position-constrained PPP with initialized variance at all 3 surveying points. To avoid the convergence of receiver clock offset and phase biases, the variance before the gap occurs is applied in position-constrained PPP and position- and ZWD-constrained PPP. The instantaneous convergence of carrier phase bias and receiver clock from inherited variance constrained PPP verifies that the ratio of weight between carrier phase bias and receiver clock after the data gaps could be considered the same as those before the gaps. There are only small displacement RMSE differences between variance-inherited position-constrained PPP and variance-initialized position-constrained PPP. The Inherited variance position- and ZWD- constrained PPP has slightly worse displacement precision performance than that from initialized variance position- and ZWD constrained PPP. This implies that better precision displacement from constrained PPP does not absolutely rely on the instantaneous convergence of carrier phase bias and receiver clock.

Table 3. RMSE of PPP bridge displacements at surveying points B, C and D.

Surveying Points	Standard (m)	Initialized (m)		Inherited (m)	
		Pos.	Pos. and ZWD	Pos.	Pos. and ZWD
Point B	1.55	0.14	0.12	0.13	0.14
Point C	0.71	0.09	0.08	0.07	0.09
Point D	0.77	0.05	0.04	0.06	0.08

4. Discussion

Standard PPP normally takes half an hour for achieving the positioning precision, before it can be used for scenarios requiring high precision. Many dataset gaps, due to the GNSS receiver signal lost and reacquired, challenge the PPP applications' feasibilities in navigation, positioning and deflection monitoring. Additional convergence time has to be taken before the PPP precision reaches the requirement. This study investigated the development of instantaneous convergence as soon as the signal was reacquired. Bridge real GNSS data, in a high-rate oscillating situation, was used for validating the improved PPP re-convergence performance. The bridge PPP experiment proves that improved PPP can instantaneously converge at the first epoch of reacquired signal. DD deflection is used as the truth of bridge deflection for assessing the improved PPP precision. The consistence of the DD and improved PPP waveforms, after the signal reacquired, proves that the improved PPP can successfully deal with all the mentioned GNSS logging gaps, with deflections biases no more than 2 cm between DD and improved PPP. It is necessary to be mentioned that this proposed method cannot only solve the gaps in bridge GNSS data, but also the GNSS data gaps in navigation and positioning scenario. Furthermore, the improved PPP can successfully deal with the GPS data logging gaps for instantaneous convergence as well as the gaps from other GNSS, e.g., BeiDou Navigation Satellite System (BDS) [22].

5. Conclusions

In this paper, we developed an improved PPP instantaneous convergence algorithm for applications to bridge displacement monitoring. Bridge data with logging gaps are used to assess the improved PPP algorithm. The partial unknown parameters, including the receiver clock offset, phase biases and their variances, at the first epoch of signal reacquisition are estimated under either position or position- and ZWD- constraints. These estimated partial parameters are then applied in the PPP Kalman filter for instantaneous displacement monitoring convergence. The improved PPP method requires only one receiver to precisely estimate the bridge displacement as soon as all the GPS signal is reacquired. For comparison, at least half an hour is required for standard PPP convergence to a reasonable precision for bridge monitoring. Additionally, there is no backward filter applied when dealing with the GPS data gap, so this method is simulating real-time PPP bridge monitoring.

Both position PPP and position- and ZWD-constrained PPP significantly improve the bridge displacement monitoring precision and convergence compared with the results from standard PPP. However, the receiver clock offset and phase biases still take tens of minutes to converge to stable values. The variances in both the clock offset and phase biases, before a data gap occurs, are applied for allowing better receiver clock offset and instantaneous converged phase biases after the data gaps.

The DD results were used as the true bridge displacement for assessing the displacement precision of improved PPP. The displacement RMSEs of standard PPP and constrained PPP were computed. All constrained PPPs with different strategies display evidently better displacement precision than standard PPPs. The precision differences among all constrained PPP methods are not remarkable. The displacement precision of the position- and ZWD-constrained PPP is slightly better than that of position-constrained PPP. Peaks in the DD time series are caused by the vehicle loading on the bridge. Constrained PPP can immediately retrieve the peaks as soon as all the GPS signal is reacquired, but standard PPP does not exhibit such peaks during the first 40 min.

Author Contributions: Conceptualization, X.T. and G.W.R.; methodology, X.T.; software, X.T.; validation, S.J. and X.T.; formal analysis, X.T. and S.J.; investigation, X.T.; resources, G.W.R.; data curation, G.W.R.; writing—original draft preparation, X.T.; writing—review and editing, S.J.; visualization, X.T.; supervision, S.J.; funding acquisition, X.T. All authors have read and agreed to the published version of the manuscript.

Funding: This research was funded by the Young Scientist program of the Natural Science Foundation of China (NSFC) with grant number 41704024, the Ningbo Commonweal project with grant number 2019C50017 and the Startup Foundation for Introducing Talent of NUIST with grant number 2019r034.

Acknowledgments: The authors acknowledge the IGS for providing the high-rate GPS observations, satellite clock and orbital products. The authors are very grateful to the Highways Agency, Severn River Crossing PLC, and Mott MacDonald for supporting and funding this research.

Conflicts of Interest: The authors declare no conflict of interest.

Appendix A

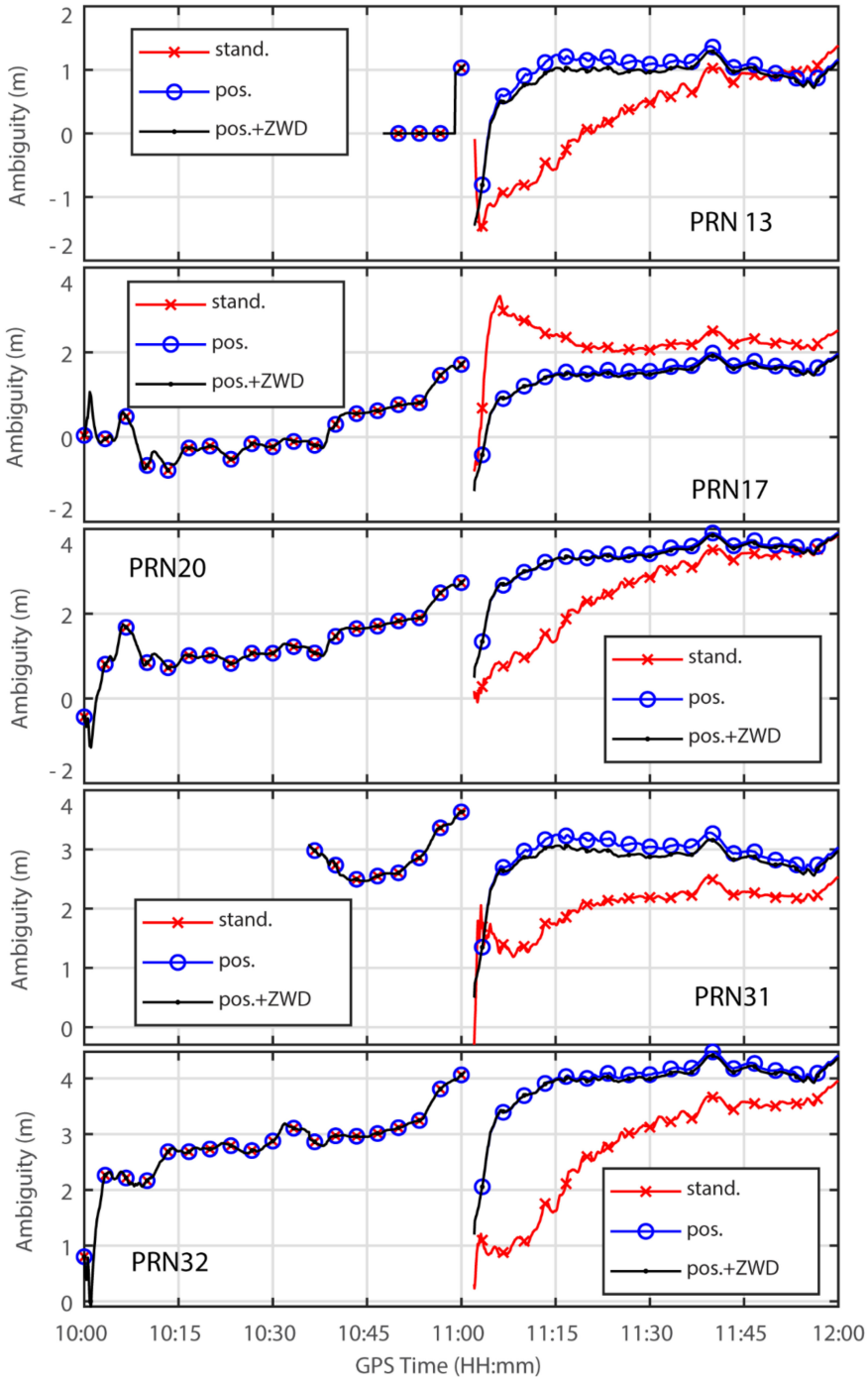

Figure A1. Zero differenced carrier phase bias solution of GPS PRN13, PRN17, PRN 20, PRN31 and PRN 32 from standard PPP and constrained PPP over 2 h.

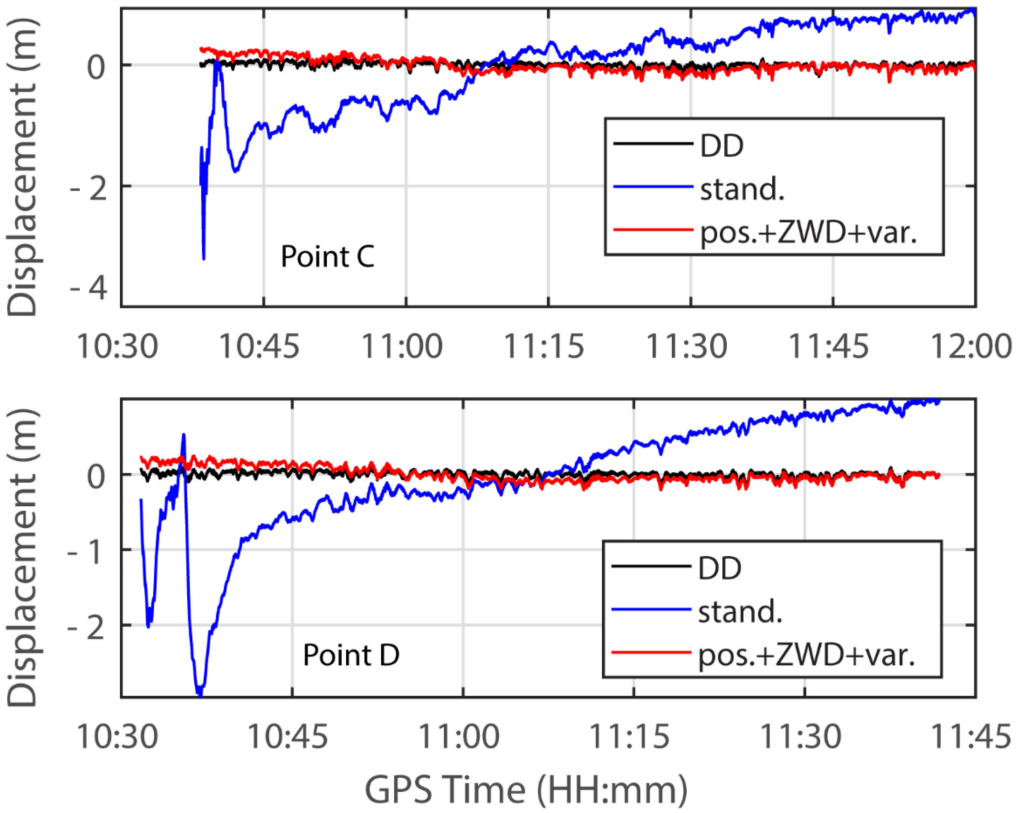

Figure A2. Comparison of position-constrained PPP and DD displacement time series after the data gap at point C (top panel) and Point D (bottom panel).

References

1. Teunissen, P.J.G.; Montenbruck, O. *Handbook of Global Navigation Satellite Systems*; Springer: Berlin, Germany, 2017.
2. Zhou, X.Y.; Jiang, W.P.; Chen, H.; Li, Z.; Liu, X. Improving the GRACE kinematic precise orbit determination through modified clock estimating. *Sensors* **2019**, *19*, 4347. [CrossRef]
3. Weinbach, U.; Schön, S. Improved GRACE kinematic orbit determination using GPS receiver clock modeling. *GPS Solut.* **2012**, *17*, 511–520. [CrossRef]
4. Geng, J.; Guo, J.; Chang, H.; Li, X. Toward global instantaneous decimeter-level positioning using tightly coupled multi-constellation and multi-frequency GNSS. *J. Geod.* **2018**, *93*, 977–991. [CrossRef]
5. Tang, X.; Hancock, C.M.; Xiang, Z.; Kong, Y.; Ligt, H.D.; Shi, H.; Quaye-Ballard, J.A. Precipitable water vapour retrieval from GPS precise point positioning and NCEP CFSv2 dataset during typhoon events. *Sensors* **2018**, *19*, 3831. [CrossRef] [PubMed]
6. Wang, J.; Liu, Z. Improving GNSS PPP accuracy through WVR PWV augmentation. *J. Geod.* **2019**, *93*, 1685–1705. [CrossRef]
7. Cai, C.S.; Liu, Z.Z.; Luo, X.M. Single-frequency ionosphere-free precise point positioning using combined GPS and GLONASS observations. *J. Navig.* **2013**, *66*, 417–434. [CrossRef]
8. Lima Filho, V.C.; Moraes, A. Modeling multifrequency GPS multipath fading in land vehicle environments. *GPS Solut.* **2020**, *25*, 1–14. [CrossRef]
9. Ge, M.; Gendt, G.; Rothacher, M.; Shi, C.; Liu, J. Resolution of GPS carrier-phase ambiguities in Precise Point Positioning (PPP) with daily observations. *J. Geod.* **2007**, *82*, 389–399. [CrossRef]
10. Zhang, B.C.; Chen, Y.C.; Yuan, Y.B. PPP-RTK based on undifferenced and uncombined observations: Theoretical and practical aspects. *J. Geod.* **2019**, *93*, 1011–1024. [CrossRef]
11. Geng, J.; Meng, X.; Dodson, A.H.; Ge, M.; Teferle, F.N. Rapid re-convergences to ambiguity-fixed solutions in precise point positioning. *J. Geod.* **2010**, *84*, 705–714. [CrossRef]
12. Vadakke Veettil, S.; Aquino, M.; Marques, H.A.; Moraes, A. Mitigation of ionospheric scintillation effects on GNSS precise point positioning (PPP) at low latitudes. *J. Geod.* **2020**, *94*, 1–10. [CrossRef]
13. Zhang, X.; Li, X. Instantaneous re-initialization in real-time kinematic PPP with cycle slip fixing. *GPS Solut.* **2011**, *16*, 315–327. [CrossRef]
14. Li, X.; Zhang, X.; Ge, M. Regional reference network augmented precise point positioning for instantaneous ambiguity resolution. *J. Geod.* **2010**, *85*, 151–158. [CrossRef]
15. Roberts, G.W.; Brown, C.J.; Tang, X.; Meng, X.; Ogundipe, O. A tale of five bridges; the use of GNSS for monitoring the deflections of bridges. *J. Appl. Geod.* **2014**, *8*, 241–264. [CrossRef]

16. Aggrey, J.; Bisnath, S. Improving GNSS PPP convergence: The case of atmospheric-constrained, multi-GNSS PPP-AR. *Sensors* **2019**, *19*, 587. [CrossRef]
17. Tang, X.; Li, X.; Roberts, G.W.; Hancock, C.M.; de Ligt, H.; Guo, F. 1Hz GPS satellites clock correction estimations to support high-rate dynamic PPP GPS applied on the severn suspension bridge for deflection detection. *GPS Solut.* **2018**, *28*, 1–12.
18. Bevis, M.; Businger, S.; Herring, T.A.; Rocken, C.; Anthes, R.A.; Ware, R.H. GPS meteorology: Remote sensing of atmospheric water vapor using the global positioning system. *J. Geophys. Res. Atmos.* **1992**, *97*, 15787–15801. [CrossRef]
19. Zumberge, J.F.; Heflin, M.B.; Jefferson, D.C.; Watkins, M.M.; Webb, F.H. Precise point positioning for the efficient and robust analysis of GPS data from large networks. *J. Geophys. Res. Sol. EA* **1997**, *102*, 5005–5017. [CrossRef]
20. Boehm, J.; Niell, A.; Tregoning, P.; Schuh, H. Global Mapping Function (GMF): A new empirical mapping function based on numerical weather model data. *Geophys. Res. Lett.* **2006**, *33*, L07304. [CrossRef]
21. Estey, L.H.; Meertens, C.M. TEQC: The multi-purpose toolkit for GPS/GLONASS data. *GPS Solut.* **1999**, *3*, 42–49. [CrossRef]
22. Jin, S.; Su, K. PPP models and performances from single- to quad-frequency BDS observations. *Satell. Navig.* **2020**, *1*, 1–13. [CrossRef]